

Probing quantum coherent states in bilayer graphene

M.J. Gilbert · J. Shumway

Published online: 23 September 2009
© Springer Science+Business Media LLC 2009

Abstract An active area of post-CMOS device research is to study the possibility of realizing and exploiting exotic quantum states in nanostructures. In this paper we consider one such system, two layers of graphene separated by an oxide insulator. This system has been predicted to have an excitonic condensate that survives above room temperature. We describe a computational technique—path integral quantum Monte Carlo (PIMC)—that directly simulates many-body quantum phenomena, including excitonic condensation. Starting from a simplified quasiparticle model, the many-body PIMC simulations show excitonic pairing and confirm a superfluid phase that persists above room temperature. We then present an atomistic PIMC model that captures more details of graphene than our quasiparticle model, and discuss how to extract parameters for a non-equilibrium Green's function calculation.

Keywords Graphene · Exciton condensate · Path integral · Quantum Monte Carlo · Superfluidity

1 Introduction

The future of device simulation appears to be a merger of materials science, electrical engineering, and quantum

physics. As technologies mature, there is increasing amount of research directed at new materials or nanostructured systems that may offer new capabilities for switching, sensing, or transporting signals. A further avenue for progress is the exploitation of exotic quantum states. Superconductors and lasers are perhaps the best-known examples of coherent quantum states with clear technological applications, but many other systems have been studied by physicists. In this paper, we discuss a coherent quantum state—an excitonic condensate—that has been predicted to exist in bilayer graphene [1–5] and has been proposed for a new switching device [6]. Our computational investigation utilizes a many-body simulation tool, path integral quantum Monte Carlo (PIMC), which is natural for studying superfluids [7], and which we have also found useful for studying quantum dots [8] and wire nanostructures.

The notion of an excitonic condensate dates back to the 1960's [9–11]. Since excitons are composed of two fermions (an electron and hole), they obey Bose statistics. At low temperatures and high densities, one may expect excitons to undergo a Bose-Einstein condensation (BEC) transition. However, exciton gases are usually meta-stable states that do not form condensates, since electron-hole recombination destroys excitons and releases energy [12]. In fact, recent experiments have had much more success studying condensation of polaritons in optical cavities [13–16]. These polaritons are hybridized exciton-photon states: bosons with very small effective masses but significant repulsive interactions. Such polariton condensates exhibit features of both excitonic condensates and lasers [17].

Another experimental system related to excitonic condensation is a bilayer quantum hall state. Over the past decade a plethora of spectacular transport effects have been experimentally observed in GaAs/AlGaAs semiconductor bilayers. These systems are in the $\nu_{\text{total}} = 1$ quantum Hall

M.J. Gilbert (✉)
Department of Electrical and Computer Engineering,
Micro and Nanotechnology Laboratory, Institute for
Cond. Mat. Theory, University of Illinois at Urbana-Champaign,
Urbana, IL 61801, USA
e-mail: matthewg@illinois.edu

J. Shumway
Department of Physics, Arizona State University, Tempe,
AZ 85287-1540, USA
e-mail: john.shumway@asu.edu

state, which means there is one electron per magnetic flux line, so each electron is bound to one magnetic flux quanta. Individually, each layer is in the $\nu = \frac{1}{2}$ state, since all the magnetic flux passes through both layers but only half the electrons are in each layer. As is the case for other quantum Hall phenomena, a strong magnetic field plays an important role of quenching the electrons' kinetic energy, allowing Coulomb interactions to play a dominant role. At these special filling factors, experiments have shown that both the longitudinal and Hall resistances vanish [18–20] when the device is biased in the counterflow geometry. Furthermore, when tunneling transport is measured at $\nu_{\text{total}} = 1$, there is a resonantly enhanced tunneling peak [21] in the differential conductance. These experiments have been interpreted as manifestations of Bose-Einstein condensation of indirectly bound excitons. The excitons are formed by making a particle-hole transformation on one of the layers in the $\nu = \frac{1}{2}$ state. This analysis assumes that the layers are spin polarized at $\nu = \frac{1}{2}$, which has been recently confirmed using optical absorption measurements [22].

The advent of graphene offers new possibilities for the realization of an excitonic condensate. Recent theoretical work [1–5] has predicted that if one were to fabricate a bilayer heterostructure using graphene monolayers, in a fashion similar to that of the semiconducting case, then for certain interlayer separations and layer carrier concentrations, the transition temperature may be well above room temperature. Bilayers of graphene are suited to the observation of BEC at much higher temperatures than semiconductor bilayers due to the fact that it is atomically two-dimensional, which enhances Coulomb interactions, and because graphene has a bandstructure that is both linear and gapless, with particle-hole symmetry.

In this paper we discuss the calculation of properties associated with excitonic superfluidity in bilayer graphene heterojunctions using the path integral Monte Carlo (PIMC) method. We find that the superfluid fraction remains saturated well beyond room temperature and we estimate the critical temperature $T_c \approx 800$ K. While our estimate is larger than the previous estimates, we attribute the difference the fact that our simple model does not include linear bands and valley degeneracy, and also to finite size effects from our periodic simulation cell. Furthermore, our calculated superfluid density, winding numbers, and pair correlation functions suggest that the transition is consistent with that of an excitonic BEC (of preformed electron-hole pairs) rather than a Bardeen-Cooper-Schrieffer (BCS) type transition, where pair formation occurs at T_c .

2 Device description

In Fig. 1 we illustrate a device geometry in which excitonic condensation may be observed. We have two monolayers of

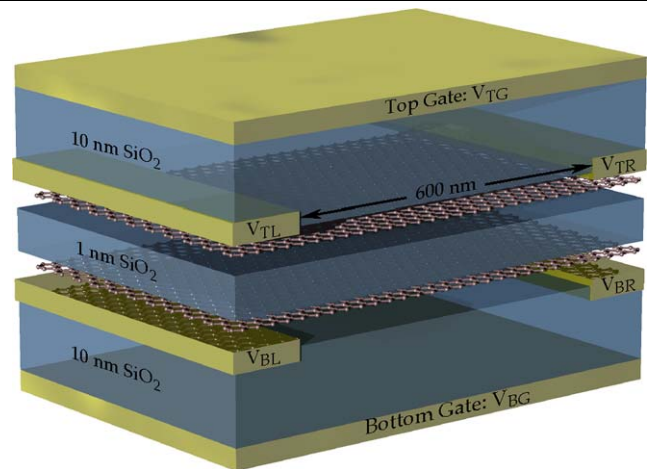


Fig. 1 Bilayer graphene tunneling device structure. Two sheets of graphene are separated by a one-nanometer thick insulating oxide layer. Electron and hole concentrations in the *top* and *bottom* layers are set by the *top* and *bottom* gates (V_{TG} and V_{BG}), and tunneling currents are driven by leads attached to the *top* and *bottom* and graphene layers (V_{TL} , V_{TR} , V_{BL} , and V_{BR})

graphene which are separated by a thin oxide barrier. Top and bottom gates (V_{TG} and V_{BG}) are used to electrostatically manipulate the quasiparticle concentrations in the top and bottom layers. The top and bottom gates are separated from the graphene layers by gate oxides which are several nanometers thick. The state can be probed by four gates, on the left and right sides of the top and bottom layers (V_{TL} , V_{TR} , V_{BL} , and V_{BR}) [1, 23]. As the phenomenon of excitonic condensation has not yet been experimentally observed in graphene bilayers, this device geometry is suggested for addressing the possible realization and detection of such a condensate.

3 The path integral quantum Monte Carlo method

A central issue, from a computational electronics perspective, is to quantitatively study the condensed state. In materials-based device models, one has an underlying Hamiltonian, such as an *ab initio* Hamiltonian for first principles atomistic simulations or a quasiparticle (effective mass) model for studying transport in semiconductor devices. In principle, the excitonic condensate emerges from the interacting particles described by the Hamiltonian. However, Bose condensation or superfluidity is inherently a many-body effect; so standard device simulations that assume weakly interacting electrons are of limited use. Instead, we utilize quantum Monte Carlo (QMC) methods that can directly simulate strongly correlated electronic systems.

In the 1980's, Ceperley and Pollock developed the PIMC method as a tool to study Bose condensation in liquid helium [7, 24]. Later work extended the method to fermions

[25], including electrons [26]. The extension to fermionic systems introduces the infamous sign-problem, which may be managed with the fixed-node approximation [25]. The fixed-node approximation takes the fermionic density matrix and maps it onto an effective bosonic density matrix which can then be easily solved with PIMC. The fixed-node approximation has been used for simulating materials under extreme conditions [27, 28], and has seen some use in simulating condensation in paired fermionic systems [29–31]. The fixed-node approximation has also been used in ground-state diffusion QMC studies of electron hole condensates [32, 33].

In the path-integral formalism of quantum statistical mechanics, the many-body thermal density matrix is represented as a sum over imaginary time paths [34],

$$\begin{aligned} \rho(R, R'; \beta) &\equiv \frac{1}{Z} \sum_i \Psi_i(R) \Psi_i^*(R') e^{-\beta E_i} \\ &= \frac{1}{Z} \int_{R(0)=R'}^{R(\beta\hbar)=R} \mathcal{D}R(\tau) e^{-\frac{1}{\hbar} S_E[R(\tau)]}. \end{aligned} \tag{1}$$

Here R represents the position coordinates of all the quantum particles, $\Psi_i(R)$ are the many-body energy eigenstates with energy E_i , $\beta = 1/k_B T$ is the inverse temperature expressed in units of inverse energy, and the partition function Z normalizes the density matrix, $\text{tr} \rho = 1$. The integral in the second line of the equation is a path integral: a sum over random walks $R(\tau)$ taking place in “imaginary time” τ , starting at R' at imaginary time $\tau = 0$ and ending at R at imaginary time $\tau = \beta\hbar$. The paths are weighted by the real-valued Euclidian action, which is a functional of the path $R(\tau)$,

$$S_E[R(\tau)] = \int_0^{\beta\hbar} \left(\frac{1}{2} m |\dot{R}|^2 + V(R(\tau)) \right) d\tau, \tag{2}$$

where $V(R)$ includes any external potentials and interactions between particles.

When computing expectation values, one takes a trace over paths, $R = R'$, so the path integral becomes a sum over closed paths. Thus the particles appear as closed loops, each about the size of the thermal de Broglie wavelength, $\lambda_{dB} = h/\sqrt{2\pi m k_B T}$. If the particles are identical, there is an additional sum over permutations,

$$\begin{aligned} \rho(R, R'; \beta) &= \frac{1}{Z} \frac{1}{N!} \sum_P (\pm 1)^P \\ &\times \int_{R(0)=R'}^{R(\beta\hbar)=PR} \mathcal{D}R(\tau) e^{-\frac{1}{\hbar} S_E[R(\tau)]}, \end{aligned} \tag{3}$$

which symmetrizes or antisymmetrizes the many-body wavefunction. The factor $(\pm 1)^P$ puts in the required plus and minus signs for permutations of bosons and fermions, respectively. If the thermal wavelength λ_{dB} is much less than

the interparticle spacing, the sum is dominated by the identity permutation. But, at low temperatures, λ_{dB} becomes large and the sum contains significant contributions from all $N!$ permutations. For bosons, the introduction of permutations leads to a percolation transition, as large chains of permuting bosons span the sample, which Feynman first identified with the superfluid phase transition [35].

When simulating fermions, the minus signs in (3) lead to an exponential inefficiency in Monte Carlo simulations, known as the fermion sign problem. We handle this with a ground-state fixed node approximation [36, 37], which we implement in the following way. At every slice on the path, we plug the electron and hole coordinates into a Slater determinant [29],

$$\det |\phi(\mathbf{r}_{e,i} - \mathbf{r}_{h,j})|, \tag{4}$$

where we have taken $\phi(r) = e^{-r/a}$ as an s-wave pairing wavefunction and we have set $a = 2.3$ nm. In sampling, we reject all paths that cross the nodes of this wavefunction. That is, we exclude from the path integral (3) any paths $R(\tau)$ in which the Slater determinant (4) changes sign. This effectively eliminates all the negative terms, giving an approximate solution to the fermionic path integral. This choice of nodal surface (4) is based on our earlier work with three-dimensional exciton condensates [29], and we base the pairing function $\phi(r)$ on an excitonic wavefunction.

There are several reasons why the PIMC approach is useful for simulating electronic systems. The first is that this is a true many-body formalism. Quantum mechanics is often applied at a single particle level, using three-dimensional wavefunctions in the Schrödinger equation or matrices representing three-dimensional basis sets. Such approaches are approximations that often require many-body effects to be reintroduced by hand. In Refs. [2, 23, 38], for instance, all effects of Coulomb interactions are ignored except for an enhancement of interlayer tunneling that emerges from a mean-field treatment of Bose condensation. In those treatments of bilayer graphene, one neglects all interactions except for an “on-site” Coulomb interaction for an electron and hole adjacent to each other, but in opposite layers. In the path integral approach, no single-particle approximation is made, so many-body effects emerge naturally. This is especially important for the problem at hand, since condensation of excitons in bilayer graphene is a many-body quantum effect.

Moreover, the path integral naturally averages over all quantum and thermal fluctuations. In (1), the thermal sum over many-body energy eigenstates is implicit in the path integral; one never computes the individual energy eigenstates. In a sense, this is what gives PIMC its power: rather than spending computer time finding the many-body energies and wavefunctions for each eigenstate individually, the focus instead is on the direct calculation of observables in

the canonical ensemble. This is particularly important for the simulations considered here, as thermal fluctuations play a critical role in determining the stability of the superfluid phase and the temperature of the superfluid transition.

One of the major benefits of the PIMC technique is that the imaginary-time path integral lends itself to efficient evaluation on high-performance computers. In a PIMC calculation [7], the many-body path, $R(\tau)$, is stored in array of size $N \times N_{\text{dim}} \times N_{\text{slice}}$, where N is the number of particles, $N_{\text{dim}} = 1, 2, \text{ or } 3$, is the number of spatial dimensions, and N_{slice} is the number of slices in imaginary time. For a simulation in at room temperature, the imaginary time path extends for a duration $\beta\hbar \sim 1$ ps, which we discretize with $N_{\text{slice}} = 256$ slices. Lower temperature simulations require longer paths and more slices. The atomistic PIMC methods that we describe in Sect. 4.3 have even more slices, in the thousands, needed to resolve electron-nuclear interactions and handle higher electron densities. The path integral (1) is sampled with Monte Carlo integration, and the algorithm is easily parallelized to dozens or even hundreds of processors. This is achieved by dividing N_{slices} over several processors (“workers”) and by using embarrassingly parallel collection of Monte Carlo data over multiple clones with different random number streams. The simulations scale as $\mathcal{O}(N^2)$ due to the Coulomb interactions in the action, or order $\mathcal{O}(N^3)$ when Slater determinants are used for the fixed-node approximation.

4 Condensate fraction and superfluid density

Bose condensation is the macroscopic occupation of a large number of particles in a single quantum state. For non-interacting particles, this idea flows naturally from the Bose-Einstein distribution, but for interacting Bose particles (such as helium atoms or excitons) the concept is more subtle. Essentially, interacting particles in a condensate do try to occupy the same single-particle state, but they also must avoid overlapping to reduce potential energy. These competing ideas manifest themselves in a many-body wavefunction, but the essence of the many-body state can be described by the *condensate fraction* and *condensate wavefunction*.

To define the condensate wavefunction for the bilayer system, one begins by constructing the one-particle density matrix,

$$\rho_1(\mathbf{r}, \mathbf{r}') = \langle \psi_T^\dagger(\mathbf{r}) \psi_B(\mathbf{r}) \psi_T(\mathbf{r}') \psi_B^\dagger(\mathbf{r}') \rangle. \quad (5)$$

Here the angle brackets indicate an expectation value over the many-body wavefunction and a thermal average. The eigenvectors of the one-particle thermal density matrix are the natural orbitals, and the eigenvalues are the fractional occupations. If there is a condensate, one orbital will have

a large occupation; this orbital is the condensate wavefunction, and its occupation is the condensate fraction. Note that the condensate fraction of an interacting system will be less than 100% even at $T = 0$, reflecting the need for particles to avoid each other in the interacting wavefunction.

In PIMC, the off-diagonal density matrix may be sampled from an open path [7]. In this approach, one would open one electron path and one hole path. If a condensate is present, the density matrix would have non-zero contributions when the open ends an electron and hole pair are far from each other. Since the diffusion of a particle in imaginary-time only extends one thermal de Broglie wavelength, $\lambda_{\text{dB}} = h/\sqrt{2\pi mk_B T}$, a condensate requires multiple excitons to permute together in long chains [7, 29].

As a mathematical shorthand, condensation is occasionally referred to as spontaneous symmetry breaking,

$$\phi(\mathbf{r}) \equiv \langle \psi_T(\mathbf{r}) \psi_B^\dagger(\mathbf{r}) \rangle \neq 0. \quad (6)$$

This is convenient because of the formal similarity to other order parameters that occur at phase transitions, such as spontaneous magnetization. However, (6) is incorrect because it requires the system to be in a quantum superposition of many different numbers of excitons. This is an artificial constraint, since an excitonic condensates can exist in an eigenstate of known N_e and N_h . In fact, if tunneling is neglected as in Ref. [2], then N_e and N_h are perfectly good quantum numbers. The condensate fraction from the long range order in (5) is meaningful in that case, while the shorthand $\phi(\mathbf{r})$ in (6) is identically zero. Nevertheless, the shorthand $\phi(\mathbf{r})$ can be a convenient theoretical device, as long as care is taken when ascribing physical meaning to the results.

In our path integral simulations, we use the superfluid density as an order parameter to establish the critical temperature for excitonic condensation. Superfluid density is the fraction of the material that stays at rest when the system is moved slowly (as in a torsion pendulum) [39]. Unlike the condensate fraction, the superfluid fraction (ρ_s/ρ) approaches 100% at low temperature. Superfluid fraction is a good order parameter: it is zero above T_c and increases monotonically from zero below T_c , finally reaching a saturated value of unity at low temperatures.

In these calculations, we use quasi-particle PIMC simulations. In quasiparticle PIMC simulations, we simulate the electron and hole quasi-particles, rather than an explicit atomistic model, allowing much larger simulation cells. Such calculations have been used to study three-dimensional electron-hole condensates in model semiconductors [30] and two-dimensional condensates in quantum well structures [32, 33]. This ability to simulate larger cells comes at a price, as the simulation of the graphene quasiparticle Hamiltonian, which has the form of a Dirac Hamiltonian [40],

$$H_{\text{Dirac}} = (-i\hbar v_f \boldsymbol{\alpha} \cdot \nabla), \quad (7)$$

is not amenable to PIMC methods. Instead we model graphene as a parabolic semiconductor with identical electron and hole masses. Furthermore, in our constant-number simulations we are unable to include electron-hole recombination, so tunneling between layers is not explicitly included in the simulations. However, the single particle tunneling amplitude is expected to be quite small in these systems, so eliminating single particle tunneling should not qualitatively change our results. Instead, the Coulomb enhancement of tunneling in quasi-particle PIMC must be inferred from analysis of interlayer correlation of electrons and holes.

In the quasi-particle model of a symmetric electron-hole bilayer with identical parabolic bands, the Hamiltonian is [33],

$$H = \sum_{i=1}^{N_e} \frac{p_{i,e}^2}{2m^*} + \sum_{i=1}^{N_h} \frac{p_{i,h}^2}{2m^*} + \sum_{i < j} \frac{e^2}{\epsilon |\mathbf{r}_{i,e} - \mathbf{r}_{j,e}|} + \sum_{i < j} \frac{e^2}{\epsilon |\mathbf{r}_{i,h} - \mathbf{r}_{j,h}|} - \sum_{i,j} \frac{e^2}{\epsilon \sqrt{|\mathbf{r}_{i,e} - \mathbf{r}_{j,h}|^2 + d^2}}. \quad (8)$$

We take $\epsilon = 3.9$, corresponding to SiO₂ barriers. To set the effective mass, we require that the Fermi velocity match the quasi-particle velocity of graphene, $v_F = 10^8$ cm/s [41]. For a two-dimensional electron (or hole) density n_e , this condition gives an effective mass,

$$m^* = \hbar \sqrt{\frac{4\pi n}{g v_F^2}}, \quad (9)$$

where g is the degeneracy due to spin and sub-lattice degrees of freedom. For graphene, $g = 4$, but to simplify our the superfluid analysis we have restricted ourselves to $g = 1$. For a density $n = 5 \times 10^{12}$ cm⁻² and $v = 1$, (9) gives $m^* = 0.09 m_e$.

In Fig. 2 we begin our analysis of superfluidity in bilayer graphene systems by examining the path permutations for a graphene bilayer with layer electron and hole concentrations of $n_e = n_h = 5 \times 10^{12}$ cm⁻², which are well within the range of densities sustainable in monolayers of graphene. One advantage of the quasiparticle PIMC technique is that Bose-Einstein condensation of excitons can be directly simulated. An excitonic superfluid appears as long permuting paths that wind around the periodic boundaries of the simulation cell [7, 30]. In Fig. 2 we show electron and hole paths for a graphene bilayer with interlayer spacing $d = 0.5$ nm. The simulation cell is a periodic square 20 nm in length, containing 20 electron-hole pairs. In Fig. 2(a), the temperature is 1200 K and we see excitons, which appear as nearby (paired) electron and hole trajectories. The localization of the paths (as small loops) shows that we have not crossed the superfluid phase boundary. In Fig. 2(b), the temperature is reduced to 300 K while we keep the density in the top and

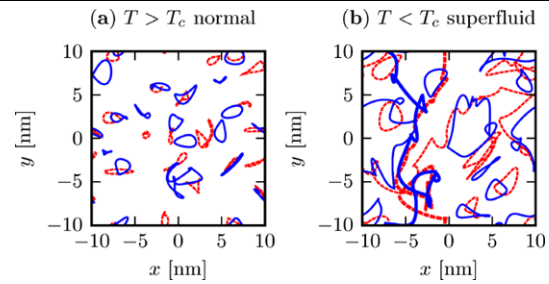


Fig. 2 (Color online) Typical paths for electrons and holes in a quasiparticle PIMC simulation of bilayer graphene with $d = 0.5$ nm. In this figure, the red dashed lines represent hole quasi-particles and the blue solid lines represent electron quasi-particles. Excitons appear as nearby electron and hole paths. (a) At temperatures above T_c , particle paths are localized by the thermal wavelength ($\hbar/\sqrt{2\pi m k_B T}$) and do not connect around the periodic boundary conditions, indicating the absence of a superfluid. (b) At temperatures below T_c , the bosonic excitons condense, as revealed by long permuting chains (shown with thicker lines) that wrap around the periodic simulation cell

bottom layers constant. Here we see that the paths now form long chains which permute around the periodic boundary conditions of our cell, indicating that we are below T_c . We have highlighted such a permuting electron-hole path with a thicker line in Fig. 2(b). This path behavior is an indication of the long range order in the thermal density matrix that suggests excitonic superfluidity.

4.1 Excitonic pairing

While Fig. 2 provides insight into the behavior of the paths above and below T_c , we wish to perform a more qualitative analysis for the formation of excitonic pairs. Furthermore, we also desire a way of distinguishing the transition as being that of a neutral excitonic superfluid or that of a charge-carrying supercurrent. To accomplish this we analyze the statistics of the winding numbers for the electrons and holes in the system. For a system of N bosons in a cubic box with side length L , the superfluid fraction is given by [7],

$$\frac{\rho_s}{\rho} = N_{\text{dim}} \frac{m T L^2}{N} \langle W^2 \rangle, \quad (10)$$

where W are topological winding numbers of the path configurations, written as dimensionless integers. In two dimensions, this simplifies to only depend on the density, boson mass, and temperature,

$$\frac{\rho_s}{\rho} = \frac{2mT}{n} \langle W^2 \rangle. \quad (11)$$

For our room-temperature simulations performed above with electron and hole densities of $n_e = n_h = 5 \times 10^{12}$ cm⁻², by utilizing an effective mass of $m = 2 \times 0.09 m_e$ (11) simplifies to $\rho_s/\rho \approx 1.22 \langle W^2 \rangle$.

In practice, we collect separate winding statistics for electrons and holes, as a histogram of probabilities,

$$P(W_{h,x}, W_{h,y}, W_{e,x}, W_{e,y}), \quad (12)$$

which we collect in a four-dimensional array in the PIMC simulations.

Using the winding histogram (12), we calculate the average,

$$\langle W^2 \rangle = \frac{1}{4} \langle (W_{h,x} + W_{e,x})^2 + (W_{h,y} + W_{e,y})^2 \rangle. \quad (13)$$

For analysis, we separate the winding histogram (12) into the sum and difference of the exciton winding: the “exciton-coupled” sum of winding numbers,

$$P(W_{h,x} + W_{e,x}, W_{h,y} + W_{e,y}), \quad (14)$$

and the “charge-coupled” difference of winding numbers,

$$P(W_{h,x} - W_{e,x}, W_{h,y} - W_{e,y}). \quad (15)$$

If the electrons and holes were very tightly bound together, then the electron and hole windings would be identical for all path configurations. In that case, the exciton-coupled winding would be distributed over even winding numbers, while the charge coupling would be zero. The squared width of the exciton-couple winding distribution (13) is proportional to the superfluid density.

In Fig. 3, we plot both the (a) “exciton-coupled” (14) and (b) the “charge-coupled” (15) winding probabilities. This figure demonstrates that we are seeing an exciton condensate. First, note that exciton-coupled windings are more pronounced for even values, consistent with windings of electron-hole pairs. Second, Fig. 3(a) shows a broad distribution of windings, not just a peak at zero winding. Using (11), we estimate the superfluid fraction to be $\rho_s/\rho \approx 0.98$. Note that the charge coupled winding, Fig. 3(b), only has a peak at zero winding, indicating the absence of a charge-carrying supercurrent.

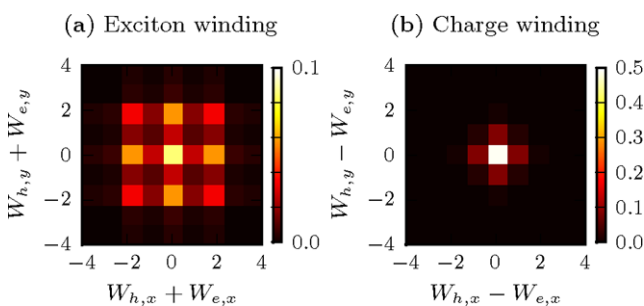


Fig. 3 (a) Exciton-coupled winding probability and (b) charge-couple winding probability at room temperature, calculated for small interlayer separation. From (11), the superfluid fraction for the exciton winding shown in (a) is $\rho_s/\rho \approx 0.98$

For excitonic system in the normal state, one can think of excitons as preformed bosons. This is especially true in dilute systems, where one can consider a weakly interacting gas of excitons. In such a system, at very low temperatures, excitons have been theoretically predicted to become quantum degenerate and condensed, but such behavior is hardly ever observed in experiments. At higher densities, one could imagine that exciton-exciton repulsion breaks up excitons, leading to a BCS scenario, where condensation drives excitonic pairing. One crucial difference between BEC and BCS is the role of interaction strength in T_c . In the strong BEC limit, where one can consider a gas of bosonic exciton, T_c is set by quantum degeneracy, which depends on the temperature, density and mass of the excitons, but not their size. In the BCS limit, interactions are crucial to the stabilization of a paired state, and T_c is strongly dependent on the strength of the pairing interaction.

One way to study exciton formation and other correlation between layers is to look at a pair correlation function,

$$n_{he}(|\mathbf{r} - \mathbf{r}_0|) = \frac{\langle n_h(\mathbf{r})n_e(\mathbf{r}_0) \rangle}{\langle n_e(\mathbf{r}_0) \rangle}, \quad (16)$$

that is, the average density of holes at point \mathbf{r} when an electron is at point \mathbf{r}_0 . Here the $n_e(\mathbf{r}_0)$ and $n_h(\mathbf{r})$ are quantum mechanical density operators, i.e., $n_e(\mathbf{r}_0) = a^\dagger(\mathbf{r}_0)a(\mathbf{r}_0)$. Since we constrain electrons and holes to be in their respective layers ($z = \pm d/2$) in the quasiparticle model, the correlation function only depends on the in-plane separation,

$$\rho = \sqrt{(x_h - x_e)^2 + (y_h - y_e)^2}. \quad (17)$$

We also define intra-layer correlation functions n_{ee} and n_{hh} , analogous to (16).

Figure 4 shows the pair-correlation functions for interlayer separations of $d = 0.5, 1, 1.5,$ and 2 nm. In our model calculations, we see evidence of excitonic pairing. The formation of excitons causes a peak in the electron hole pair correlation function, n_{he} , near $\rho = 0$, which we see clearly in Fig. 4(a). We see that the peak then begins to decay significantly when we increase the interlayer separation.

4.2 Temperature dependence of condensation

Because we are using a finite-temperature many-body method, we can directly simulate the relevant temperatures to determine the phase diagram. To this end, we calculate the superfluid density at a range of temperatures and interlayer separations.

In Fig. 5, we plot the superfluid density versus the system temperature by taking 20 electron-hole pairs in a $20 \text{ nm} \times 20 \text{ nm}$ periodic supercell, at temperatures of 150, 300, 600, and 1200 K. We find that the superfluid fractions are essentially the same for the different interlayer separations we

Fig. 4 Pair correlation functions n_{he} and n_{ee} , defined in (16), for different interlayer separations, d . The solid line show intra-layer correlation ($n_{ee} = n_{hh}$), showing the exchange-correlation hole. The dashed line is the inter-layer correlation $n_{he}(\rho)$, which is enhanced by excitonic binding of electrons and holes

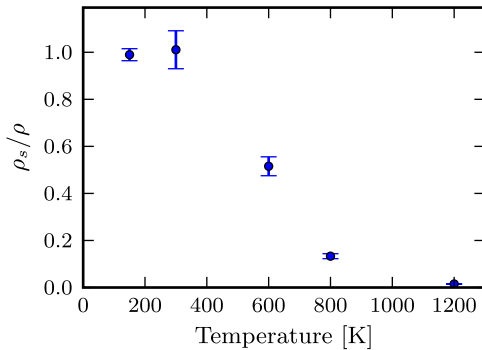
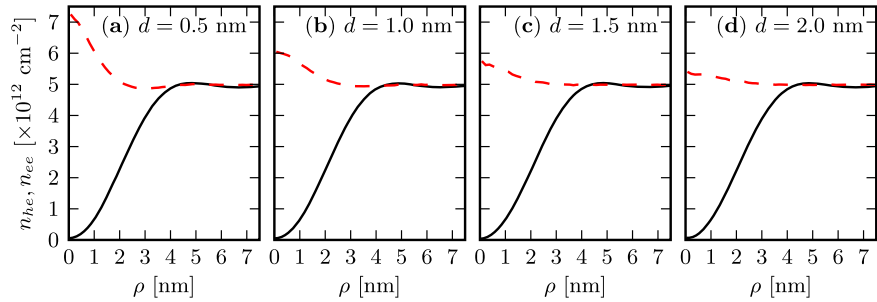


Fig. 5 Superfluid fraction ρ_s/ρ versus temperature from quasi-particle simulations of graphene, with $n = 5 \times 10^{12} \text{ cm}^{-2}$. Errorbars are statistical error from Monte Carlo sampling. In contrast to the pair correlation functions, Fig. 4, we find the calculated superfluid densities are nearly independent of layer separation for d between 0.5 and 5.0 nm, so we only show the average of all calculations. From this graph we estimate that $T_c \approx 800 \text{ K}$, but consideration of finite size effects and valley degeneracy would lower this estimate by about a factor of two

have studied, so we plot the average of all the simulation data in the figure. We see that the fraction of superfluid density is zero for $T = 1200 \text{ K}$ and then rises smoothly to saturation. From this figure, we estimate that the superfluid fraction vanishes around 800 K, giving $T_c \approx 800 \text{ K}$.

In our estimates of the superfluid fraction ρ_s/ρ , we find the somewhat surprising result that the superfluid fraction only depends on temperature, not interlayer separation for d in the range 0.5 to 5 nm. This can be understood if the system is in the BEC limit. The interlayer separation affects electron-hole interaction strength, and hence the size of the excitons. However, in the BEC limit, T_c is roughly independent of the size of the bosons. If we take the superfluid fraction to be a good indicator of T_c , then our results support our interpretation of this model being in the BEC limit.

We note that our estimates of T_c are approximately two times larger than the previously predicted estimates [2]. We have not accounted for finite size effects, which typically lead to estimates of T_c that are too high in smaller systems. Since some fluctuations are suppressed by forcing the system into a small periodic box, the ordered superfluid state is more favorable with small system sizes. Viewed another

way, in small simulation cells there may be some extra winding not associated with long permuting paths and condensate formation, which leads to an artificial increase in our superfluid estimate (11). A further source of discrepancy lies in some of the assumptions in our simplified quasiparticle model. We can comment on the effect of spin and valley degeneracy, which we have neglected by setting $g = 1$ in (9). If we assume that excitons do not interact strongly, then the extra degeneracy would lower quantum degeneracy, thus lowering the transition temperature. Since (dimensionally) T_c scales as density (since $\lambda_{dB} \sim T^{-1/2}$), a factor of two for valley degeneracy would lower our T_c by a corresponding factor of two.

4.3 Looking beyond the quasiparticle model

While the results of the previous section provide insights into excitonic condensation in the bilayer system, we would like to move beyond some of the limitations of our quasiparticle model. To this end, we are working on new atomistic PIMC simulations of graphene bilayers that will capture all the effects of the Dirac Hamiltonian. An end goal of this new work is to extract the tunneling enhancement term for realistic device parameters to precondition NEGF based simulations of the condensate flow [1, 23] beyond the linear response regime. These atomistic simulations should include all relevant details of the Dirac Hamiltonian (7) capture many-body electron-hole interactions, and describe excitonic BEC and superfluidity.

The electronic behavior of a graphene arises from out-of-plane p_z -orbitals that form π -bonds. This is well-captured by a tight binding model with one orbital on each site of a hexagonal lattice with bond-length $a = 1.42 \text{ \AA}$ and a hopping energy of $t = 2.8 \text{ eV}$ [40]. The Dirac Hamiltonian (7) can be derived by linearizing the tight-binding solution around the Fermi points. For consideration of electron-electron interactions, the systems can be modeled as a Hubbard model with onsite interaction energy $U \approx 10 \text{ eV}$ [40].

The Dirac Hamiltonian (7) is not amenable to the PIMC techniques from Sect. 3, since there is a possibility of particle-hole creation and an explicit spin-dependence introduced by chirality. Instead, we can apply PIMC to a tight-binding model, from which the Dirac physics naturally

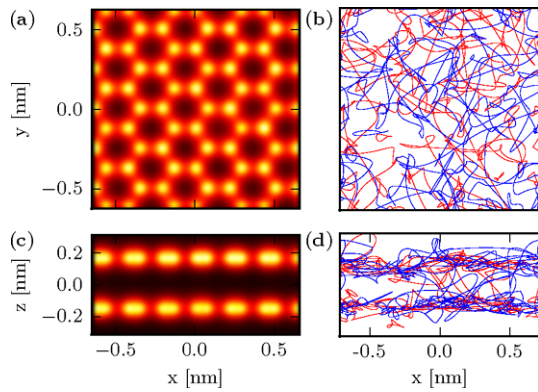


Fig. 6 (Color online) Charge densities—(a) and (c)—and typical paths—(b) and (d)—from atomistic PIMC simulations of interacting electrons in bilayer graphene. Here graphene is modeled with one orbital per atom, corresponding to the electronically active out-of-plane carbon $2p_z$ orbitals. In this figure, the *red paths* represent spin up electrons and the *blue paths* represent spin down electrons. Charge densities are collected as a Monte Carlo sum over many such paths. An electric field in the $-z$ direction (applied with the top and bottom gates in Fig. 1) has pushed 0.6 electrons from the bottom layer to top layer, corresponding to a carrier density (electrons quasiparticles in the top layer and hole quasiparticles in the bottom layer) of $4 \times 10^{11} \text{ cm}^{-2}$

emerges. Since we are working with continuum methods, but only want one orbital per atom, we make a graphene model from hydrogen atoms arranged on a hexagonal lattice. To calibrate our hydrogenic model, we have extracted effective t and U parameters from a hydrogen dimer and find $t \approx 2.7 \text{ eV}$ and $U - V \approx 4.5 \text{ eV}$, where V is the nearest-neighbor potential energy. These numbers were estimated by simulating bosonic electrons in a dimer with protons fixed a distance 1.42 \AA apart and collecting statistics on the path permutations and double occupancy, following the method in Ref. [42]. At this level of approximation, which neglects dielectric screening by valence electrons in sigma bonds and core electrons, these values of t and U are quite reasonable, and we have not considered further refinements, such as modifying the electron mass. In Fig. 6 we show charge densities and typical imaginary-time paths from a PIMC simulation of bilayer graphene. For these initial calculations, we limited the periodic simulation cell to 120 electrons, and artificially decreased the interlayer separation to scale with the small simulation cell.

In the path-integral formalism, tunneling appears as instants: rapid crossing of paths between potential minima. In Fig. 6(d), one can see several paths crossing between layers. Quantitative extraction of U from these simulation will require solution to several unresolved problems: (i) we have to verify that condensation is indeed occurring within the fixed-node approximation, (ii) the effects of bare tunneling and correlation enhanced tunneling may have to be separated in the analysis of the PIMC data, and (iii) finite size-scaling will have to be considered, as mentioned previously.

To calculate the on-site Coulomb term, we plan to examine the interacting interlayer conductivity versus the non-interacting interlayer conductivity. The ratio of these values will give us the interaction enhancement of the tunneling which will become part of the on-site term we desire. To calculate the interlayer conductivity, we work with the imaginary time current-current correlation functions. These correlations functions then may be used in the Kubo formula for the electrical conductivity. The current-current correlation function may be collected by watching the paths fluctuate between the two layers, as seen in Fig. 6. Here we see paths fluctuating from the top and bottom, indicating particle transfer between the layers. When the system is at spontaneous coherence, we expect typical values of the exchange coupling between the layers to be $\sim 10\%$ of the system Fermi energy [2].

5 Conclusion

In this paper, we have described the use of path integral quantum Monte Carlo to study the existence, stability and pairing nature of excitonic superfluids in bilayer graphene through the use of a simplified quasi-particle model. From the superfluid density, Fig. 5, we find that the transition temperature, T_c , for doped electron-hole bilayer graphene is well above room temperature. Here, we estimate the critical temperature to be $T_c \approx 800 \text{ K}$. However, this analysis likely overestimates T_c due to the fact that we are working with a small simulation cell, have neglected valley degeneracy, and approximate graphene with parabolic bands. We show by calculating the topologically invariant winding numbers and pair correlation functions that the transition is consistent with that of a BEC of neutral excitons rather than a charged superfluid. We find that the superfluid density depends only on the temperature of the system and not on the specifics of the interlayer spacing between the two graphene layers. This result is further evidence that the transition we see is that of a BEC of pre-formed excitons. Finally, we have presented initial work on the use of atomistic PIMC to compute interlayer coupling at and below interlayer phase coherence to not only check the results given by the quasi-particle model but to estimate the strength of the on-site Coulomb term to precondition the mean-field Hamiltonian in NEGF based simulations of the condensate dynamics.

Acknowledgements Work supported by SRC-NRI South West Academy of Nanoelectronics and the Army Research Office. Computer simulations were supported through NSF TeraGrid resources provided by NCSA, LONI, and TACC, as well as computer resources from the Fulton Center for High Performance computing.

References

1. Su, J.J., MacDonald, A.H.: Nature Physics **4**, 799 (2008)

2. Min, H., Bistrizter, R., Su, J.J., MacDonald, A.H.: Phys. Rev. B **78**, 121401 (2008)
3. Milovanović, M.V.: Phys. Rev. B **78**(24), 245424 (2008)
4. Bergman, D.L., Hur, K.L.: Phys. Rev. B **79**(18), 184520 (2009)
5. Zhang, C.H., Joglekar, Y.N.: Phys. Rev. B **77**, 233405 (2008)
6. Banerjee, S.K., Register, L.F., Tutuc, E., Reddy, D., MacDonald, A.H.: IEEE Electron Device Lett. **30**, 158 (2009)
7. Ceperley, D.M.: Rev. Mod. Phys. **67**, 279 (1995)
8. Wimmer, M., Nair, S.V., Shumway, J.: Phys. Rev. B **73**(16), 165305 (2006)
9. Moskalenko, S.A.: Sov. Phys. Solid State **4**, 199 (1962)
10. Blatt, J.M.: Phys. Rev. **126**, 1691 (1962)
11. Keldysh, L.V., Kozlov, A.N.: Sov. Phys. JETP **27**, 521 (1968)
12. O'Hara, K.E., Süilleabháin, L. Ó, Wolfe, J.P.: Phys. Rev. B **60**, 10565 (1999)
13. Kasprzak, J., Richard, M., Kundermann, S., Baas, A., Jeambrun, P., Keeling, J.M.J., Marchetti, F.M., Szymaska, M.H., André, R., Staehli, J.L., Savona, V., Littlewood, P.B., Deveaud, B., Dang, L.S.: Nature **443**, 309 (2006)
14. Balili, R., Hartwell, V., Snoke, D., Pfeiffer, L., West, K.: Science **316**, 1007 (2007)
15. Utsunomiya, S., Tian, L., Roumpos, G., Lai, C.W., Kumada, N., Fujisawa, T., Kuwata-Gonokami, M., Löffler, A., Höfling, S., Forchel, A., Yamamoto, Y.: Nature Physics **4**, 700 (2008)
16. Amo, A., Sanvitto, D., Laussy, F.P., Ballarini, D., del Valle, E., Martin, M.D., Lemaître, A., Bloch, J., Krizhanovskii, D.N., Skolnick, M.S., Tejedo, C., Vifia, L.: Nature **457**, 291 (2008)
17. Snoke, D.: Science **298**, 1368 (2002)
18. Kellogg, M., Eisenstein, J.P., Pfeiffer, L.N., West, K.W.: Phys. Rev. Lett. **93**, 036801 (2004)
19. Tutuc, E., Shayegan, M., Huse, D.A.: Phys. Rev. Lett. **93**, 246603 (2004)
20. Wiersma, R.D., Lok, J.G.S., Kraus, S., Dietsche, W., Von Klitzing, K., Schuh, D., Bichler, M., Tranitz, H.P., Wegscheider, W.: Phys. Rev. Lett. **93**, 266805 (2004)
21. Spielman, I.B., Eisenstein, J.P., Pfeiffer, L.N., West, K.W.: Phys. Rev. Lett. **84**, 5808 (2000)
22. Plochocka, P., Schneider, J.M., Maude, D., Potemski, M., Rappaport, M., Umansky, V., Bar-Joseph, I., Groshaus, J.G., Gallus, Y., Pinczuk, A.: Phys. Rev. Lett. **102**, 126806 (2009)
23. Gilbert, M.J.: Submitted to Appl. Phys. Lett. (2009)
24. Pollock, E.L., Ceperley, D.M.: Phys. Rev. B **30**(5), 2555 (1984)
25. Ceperley, D.M.: Phys. Rev. Lett. **69**, 331 (1992)
26. Pierleoni, C., Ceperley, D.M., Bernu, B., Magro, W.R.: Phys. Rev. Lett. **73**(16), 2145 (1994)
27. Magro, W.R., Ceperley, D.M., Pierleoni, C., Bernu, B.: Phys. Rev. Lett. **76**(8), 1240 (1996)
28. Militzer, B.: Phys. Rev. B **79**(15), 155105 (2009)
29. Shumway, J., Ceperley, D.M.: J. Phys. IV France **10**, 5 (2000)
30. Shumway, J., Ceperley, D.M.: Solid State Commun. **134**, 19 (2005)
31. Akkineni, V.K., Ceperley, D.M., Trivedi, N.: Phys. Rev. B **76**(16), 165116 (2007)
32. Zhu, X., Littlewood, P.B., Hybertsen, M.S., Rice, T.M.: Phys. Rev. Lett. **74**, 1633 (1995)
33. De Palo, S., Rapisarda, F., Senatore, G.: Phys. Rev. Lett. **88**, 206401 (2002)
34. Feynman, R.P.: Statistical Mechanics. Addison-Wesley, Reading (1972)
35. Feynman, R.P.: Phys. Rev. **91**, 1291 (1953)
36. Anderson, J.B.: J. Chem. Phys. **65**, 4121 (1976)
37. Reynolds, P.J., Ceperley, D.M., Alder, B.J., Lester, W.A.: J. Chem. Phys. **77**, 5593 (1982)
38. Seradjeh, B., Moore, J.E., Franz, M.: Phys. Rev. Lett. **103**, 066402 (2009)
39. Hess, G.B., Fairbank, W.M.: Phys. Rev. **19**, 216 (1967)
40. Neto, A.H.C., Guinea, F., Peres, N.M.R., Novoselov, K.S., Geim, A.K.: Rev. Mod. Phys. **81**(1), 109 (2009)
41. Novoselov, K.S., Geim, A.K., Morozov, S.V., Jiang, D., Katsnelson, M.I., Grigorieva, I.V., Dubonos, S.V., Firsov, A.A.: Nature **438**, 197 (2005)
42. Zhang, L., Gilbert, M.J., Pedersen, J., Shumway, J.: Path integral study of the role of correlation in exchange coupling of spins in double quantum dots and optical lattices. Unpublished. [arXiv:0809.0038](https://arxiv.org/abs/0809.0038)